The Sensitive Regions of Surface Air Temperature and Terrestrial Precipitation to Global Warming, IPO and AMO

Chengyu Xu (✉ 202212010063@nuist.edu.cn)

  NUIST: Nanjing University of Information Science and Technology   https://orcid.org/0009-0000-4325-8851

Li Tao

  NUIST: Nanjing University of Information Science and Technology   https://orcid.org/0000-0002-2644-983X

Abstract

Against the background of global warming (GW), the distribution of decadal (10−20-year), multidecadal (20−50-year) and secular (>50-year) variabilities and their causes of surface air temperature (SAT) and terrestrial precipitation were explored. We applied the singular spectrum analysis method to categorize the low-frequency variabilities of global SAT and terrestrial precipitation anomalies. Three sea surface temperature (SST) modes were identified through singular value decomposition that affect the low-frequency variabilities of global SAT and terrestrial precipitation anomalies—namely, the GW, Interdecadal Pacific Oscillation (IPO) and Atlantic Multidecadal Oscillation (AMO) modes. The sensitive regions of SAT and terrestrial precipitation to GW, IPO and AMO were validated through an information flow method. Significant decadal and multidecadal variabilities of SAT were found to exist over the Pacific and Northern Atlantic, respectively, because of the IPO and AMO. In terms of terrestrial precipitation, a large area with a wet trend was found over Eurasia at mid-to-high latitudes, and this trend was especially remarkable in the boreal winter half-year (November−April), as compared with that in the boreal summer half-year (May−October). As a result, it could be concluded that GW is the trigger of the wet trend. By employing artificial neutral networks with a self-organized map to cluster the key patterns of vertically integrated water vapor flux, we found that the synopitic circulation related to the wet trend is characterized by westerly flow that transports water vapor from the northeastern Atlantic to Eurasia, which is favorable for precipitation there both in the boreal winter and summer half-year.

1 Introduction

The world's climate becoming warmer and warmer, which we commonly refer to as global warming (GW), is broadly accepted as a clear fact (Mccrystall et al. 2021). However, the surface air temperature (SAT) is not increasing at a constant rate; rather, it shows fluctuating growth because of the combination of external forcing and internal variability of the climate system (Wei et al. 2019). The oceans are a source of low-frequency variability owing to their higher heat capacity compared to the atmosphere and land, which also affects the low-frequency variability of precipitation. Some studies have suggested that the so-called "global warming hiatus" during 1998−2013 was caused by the La Niña-dominated conditions in the Pacific (Kosaka and Xie 2013; Meehl et al. 2013; Meehl et al. 2016) a mode called the Pacific Decadal Oscillation (PDO; Mantua et al. 1997; Zhang et al. 1997; Minobe 1999; Chen and Wallace 2015) or the Interdecadal Pacific Oscillation (IPO; Power et al. 1999; Deser et al. 2004). Meanwhile, Chen and Tung (2014) illustrated that more heat moves into deeper layers in the Atlantic and the Southern Ocean, which is related to the warm salt subduction mechanism in the subpolar Atlantic. The contribution of the PDO to global-mean surface temperature is only 1/10 of that of the Atlantic Multidecadal Oscillation (AMO; Kushnir 1994; Schlesinger and Ramankutty 1994; Kerr 2000; Knight et al. 2005) because of the offset of cold and warm SST in the PDO's pattern (Chen and Tung 2018).

Although the global-mean water vapor increases by approximately 7% for each 1-K increase in temperature, obeying the Clausius−Clapeyron expression, the global-mean precipitation does not scale with the Clausius−Clapeyron expression, instead increasing on the order of 2% K^{-1} (e.g., Allen and Ingram

2002; Held and Soden 2006). Moreover, future changes in precipitation with GW are expected to be spatially variable, following a "warmer-gets-wetter" or "wet-gets-wetter" pattern, based on *ocean* evidence (Held and Soden 2006; Xie et al. 2010). Meanwhile, Greve et al. (2014) found that only 10.8% of the global *land* area shows a robust "wet-gets-wetter, dry-gets-drier" pattern, based on combinations of hydrological datasets during 1948–2005. Furthermore, by virtue of the so-called "polar amplification effect" (Serreze and Francis 2006; IPCC 2007; Screen and Simmonds 2010), at local scales, precipitation has experienced an unprecedented increase and is projected to intensify throughout the 21st century along with increased evaporation from expanding open water areas (Bintanja and Selten 2014; Bintanja and Andry 2017; Mccrystall et al. 2021). And besides anthropogenic climate change (Held et al. 2005), it is believed that, during the positive (negative) phase of the AMO, the precipitation over the Sahel is enhanced (suppressed) and suppressed (enhanced) over the Gulf of Guinea (Mohino et al. 2011). Indeed, climate models have verified a causal link between the AMO and the Sahel summer rainfall (Zhang and Delworth 2006). In addition, Mccabe et al. (2004) documented that more than half of the drought frequency in the conterminous U.S. is attributable to the PDO and AMO, and a positive phase of the AMO in combination with a negative phase of the PDO is associated with a high probability of drought events. Elsewhere, Li et al. (2010) suggested that El Niño-like warming in the tropical Pacific can lead to weakened summer monsoons and thus drier conditions in East China; and in fact, the interdecadal variability of the global-mean precipitation in the past few decades is relatively stronger than the trend (Allen and Ingram 2002; Gu and Adler 2013), as well as the tropical-mean precipitation (Gu et al. 2007; John et al. 2009).

Tao et al. (2021) identified that the dominant modes affecting the interdecadal variability of terrestrial precipitation differ from season to season. The dominant modes affecting North American precipitation are the AMO and IPO in summer and the IPO and AMO in winter (Xu et al. 2021), while those affecting East Asian precipitation are GW and the IPO in both summer and winter (Du et al. 2022). However, previous studies have not presented the distribution of the relative magnitude of the decadal variability, multidecadal variability, and secular trend in SAT and terrestrial precipitation anomalies across the globe. In this study, we addressed this knowledge gap by applying singular spectrum analysis (SSA; Vautard and Ghil 1989). Furthermore, by employing the information flow analysis method recently developed by Liang (2014), we sought to identify the sensitive regions where GW, the IPO or the AMO can significantly affect the SAT and terrestrial precipitation. In particular, because of a relative dearth of studies, we focused on Eurasian terrestrial precipitation at mid-to-high latitudes (EAMH). The circulation changes were investigated by constructing artificial neutral networks with a self-organizing map (SOM).

The remainder of the paper is organized as follows: Section 2 describes the data and methods. In section 3, the distributions of the relative magnitudes of the decadal variability, multidecadal variability, and secular trend in SAT anomalies across the world's land and oceans, along with their relationships with GW, the IPO and the AMO, are presented. The same procedure was applied to terrestrial precipitation anomalies and the results are presented in section 4, in which the mechanisms of the precipitation secular trend in EAMH in summer and the winter half of the year are further explained. Lastly, conclusions are given in section 5.

2 Data And Methods

2.1 Data

The data used in this study were: (1) monthly terrestrial SAT data from the Climate Research Unit (CRU) Time Series, version 4.05 (Harris et al. 2020); (2) monthly SAT data from the Goddard Institute for Space Studies (GISS), which also covers the oceans (Hansen et al. 2010); (3) monthly terrestrial precipitation data from the Global Precipitation Climatology Centre (GPCC; Schneider et al. 2022); (4) daily vertically integrated water vapor flux reanalysis data from the fifth major global reanalysis produced by the European Centre for Medium-Range Weather Forecasts (ERA5; Hersbach et al. 2020); (5) monthly SST data from the Met Office Hardley Center (Rayner et al. 2003); (6) IPO and AMO monthly time series data from Physical Sciences Laboratory of the National Oceanic and Atmospheric Administration [the IPO time series is taken from the difference between the SST anomaly (SSTA) averaged over the central equatorial Pacific and that averaged over the Northwest and Southwest Pacific; the AMO time series is estimated as the detrended-area-weighted SST averaged over the North Atlantic ($0°-70°N$); and both the AMO and IPO series were filtered with a 9-year Lanczos low-pass filter to remove the high-frequency signals (Fig. 1)]; and (7) the GW time series, defined as the trend of the global-mean SST averaged between 45°S and 60°N, obtained by applying ensemble empirical mode decomposition and presents a noticeable nonlinear upward trend, as shown in Fig. 1.

Because data (1) and (3) over some regions (e.g., the Tibetan Plateau and northern Africa) are set to climatological monthly means before 1933, the analysis period for those data was set from 1934 to 2020 to ensure data reliability. On the other hand, the time spans of data (2) and (4) were set to the maximum length available, which was from 1948 and 1950 to 2020, respectively. Meanwhile, all the gridded data were regridded to a 2° × 2° resolution, and the seasonal cycle was removed from the monthly time series as a pretreatment. For SAT, we only examined the sensitive regions of annual-mean SAT to GW, the IPO and the AMO. For the EAMH terrestrial precipitation, we carried out further investigations in different seasons owing to the fact that the atmospheric circulation in this region causing the precipitation differs from season to season. In this study, we separated the seasons into the boreal summer half-year (May−October) and boreal winter half-year (November−April).

2.2 Methods

a. SSA

At each grid point, we applied SSA (Vautard and Ghil 1989) to seperate the time series into interannual (2−10-year), decadal (10−20-year), muitidecadal (20−50-year), and secular (> 50-year) components. The SSA algorithm is analogous to the extended empirical orthogonal function (EOF) algorithm, but the former analyzes a single time series while the latter analyzes the principle component of meteorological fields. SSA performs singular value decomposition on the autocovariance matrix of a single time series using a specified lag window (M). The original time series is then decomposed into M reconstructed components (RCs) and M corresponding normalized eigenvalues. Each normalized eigenvalue measures

the fraction of total variance contributed by the RC. After testing for M, we set M to 15 years and the results were stable for a range of values between 12 and 30 years. Only the first 6 RCs were taken for analysis, because the high-order components generated by SSA are considered as noise. The dominant period of each RC was estimated using the Fourier transform (Ault and St. George 2010), and the cumulative variance of the leading RCs measures the fraction of total variance in each band.

Localized significance tests of the decadal, multidecadal and secular variability were conducted by comparing the percentage variance in each band against the percentage variance obtained from a Monte Carlo analysis of 10 000 white noise time series with the same length as the SAT/terrestrial precipitation time series.

b. Information flow

Correlation or regression analysis are usually conducted to identify the causality between two time series. However, correlation analysis lacks directetness or asymmetry and hence does not imply causality. Liang (2014) derived an information flow formula from first principles in physics, which has been applied successfully to investigate many cause–response relationships in fields such as neuroscience, finance, and the atmospheric sciences. Information flow analysis Liang (2014) was employed in this study to identify the regions where GW, the IPO or the AMO can have a significant effect.

In a linear system, the formula is remarkably simple, involving only the common statistical covariance. Considering two time series of X_1 and X_2, the information flow from X_2 to X_1, written as $T_{2 \to 1}$, is

$$T_{2 \to 1} = \frac{C_{11} C_{12} C_{2,d1} - C_{12}^2 C_{1,d1}}{C_{11}^2 C_{22} - C_{11} C_{12}^2}$$

1

,

where C_{ij} is the sample covariance between X_i and X_j, $C_{i,dj}$ is the covariance between X_i and a derived series using Euler's forward differencing scheme:

$$\dot{X}_j = \frac{X_{j,n+1} - X_{j,n}}{\triangle t}$$

2

.

Ideally, when $T_{2 \to 1} = 0$, X_2 is not causal to X_1; otherwise, it is causal. In applications, the statistical significance should be tested. More details can be referred to in Liang (2014). The unit for $T_{2 \to 1}$ is nats per unit time.

During calculating information flow in the summer half-year, time series of different indices and the SAT/precipitation field in the winter half-year are set to zero, to avoid a large false gradient when calculating the information flow. The procedure is the same in the winter half-year.

c. SOM

An SOM was utilized in this study to categorize synoptic-scale patterns dominating the precipitation and to examine the circulation pattern changes under GW. In doing so, the aim was to understand the physical mechanisms of precipitation change.

As a relatively new pattern recognition technique or clustering algorithm, the SOM is a kind of artificial neural network with an unsupervised competitive learning mechanism. It can discover the internal laws of the input data via the adjustment of network parameters and structure to cluster data (Kohonen 1982). Most common synoptic classifications usually involve either a set of variables at a single grid point or a single variable at a regional spatial level. For the latter, one general shortcoming is that while discrete realizations of an atmospheric circulation can be represented, they generally cannot be organized into a continuum, which can be solved in an SOM. Since the successful application reported by Hewitson and Crane (2002), SOMs have been utilized in many climatological studies (Sheridan and Lee 2011).

Most previous studies usually applied SOMs to the sea level pressure or geopotential height fields first, and found their key clustering patterns. Then, the corresponding wind fields, including zonal and meridional winds, were composited to analyze their circulation. Different to this approach, we clustered the daily vertically integrated water vapor flux during 1950−2020, which includes 2D variables and is closely related to precipitation, to categorize synoptic-scale patterns directly.

The network consists of an input and a competition layer. Given an N-dimensional data space containing a cloud of input data points, the algorithm then transforms it into a 2D array composed of $a \times b$ nodes. Referring to previous studies (Zhou and Jiang 2016; Li et al. 2020; Zhou et al. 2020) and comparing square topological arrays of various sizes, we found that a 5×4 array could clearly separate the key patterns of the vertically integrated water vapor flux, and so we chose this array for studying the precipitation trend mechanism. The steps are as follows:

After vector normalization and weight initialization, in the competition layer, the input data vector X is compared with the reference vector W_j at the jth node, one by one, and the Euclidean distance between them is calculated. According to the competitive learning rule named "winner takes all", only one winning reference vector with the minimum distance between the input vector will be searched; that is, to find

$$Min\|X - W_j\|.$$

Then, the winning node begins to adjust and change the weight for itself and neighboring nodes as defined by the user. The above steps are cycled n times.

3 Sat

3.1 Decadal variability, multidecadal variability, and secular trend of global SAT

To explore the relative magnitudes of the decadal (10–20-year), multidecadal (20–50-year) and secular (>50-year) components of annual SAT at each grid point, SSA was applied to the SAT data from CRU during 1934–2020 and from GISS during 1948–2020.

As shown in FIG. 2, the decadal and multidecadal variability is relatively small for most grid points, contributing less than 20% of the total variance, while secular trends have much greater importance. Throughout most of the land area, the annual SAT does not contain any significant decadal (10–20-year) variability, but broadly significant regions exist over a large part of the Pacific, including the central tropical Pacific, central North Pacific, coastal California, the ocean areas near New Zealand, Antarctica and the southern part of the tropical Atlantic, with the variance accounting for around 30%. For the 20–50-year variability in FIG. 2c and d, relatively high variability is apparent over the Amazonian plain in South America. Roughly 60% of the SAT variance there falls within the 20–50-year band, as shown by the SAT from CRU during 1934–2020, but the signal disappears in GISS during 1948–2020 because of the locally missing data. Significant multidecadal variability over central Africa, Greenland and northern Australia can also be identified in the SAT from CRU during 1934–2020, but the contribution is less than 20%. Different from the "warm Arctic–cold continent" patterns (Zhao et al. 2022), no variability within the 20–50-year band is apparent over the region from Lake Balkhash to Lake Baikal. In terms of the oceanic SAT, there is significant multidecadal variability over the oceans near Hawaii, coastal Canada, the northern Atlantic, and ocean areas near Antarctica, where the contribution is more than one-third of the variance.

Most notably, the SAT mainly shows a unified secular trend globally across both land and ocean (FIG. 2e, f). In particular, the variance of the secular trend over Mexico, the East African Plateau, the Arabian Peninsula, the Mongolian Plateau, the Tibetan Plateau, and the Great Australian Basin, as well as over ocean areas such as the Indian Ocean, tropical West Pacific and Atlantic, accounts for up to 70%. In other words, the secular trend over the above regions is highly prominent compared to the decadal and multidecadal variability. In contrast, the realtive varaince of the secular trend is small over the central-eastern tropical Pacific, North Pacific, northern North Atlantic, northern North America, northern Eurasian continent, and northern Australia.

3.2 Dominant SST modes related to SAT low-frequency variability

The above analysis identified the significant regions of decadal variability, multidecadal varaibility and secular trends of SAT globally across both land and ocean. The unified secular trend is the foremost feature. In this section, the spatial distribution of the coupling between the decadal variability, multidecadal varaibility, secular trend of SAT and SST is investigated.

Empirical orthogonal function (EOF) analysis was performed on the global SAT from GISS for the period 1948–2020 to explore the the spatial distributions of SAT related to GW, the IPO and the AMO. Prior to the analysis, the interannual variation was removed using a 9-year Lanczos low-pass filter.

The first three modes and the corresponding principle components (PCs) are shown in FIG. 3. The variances are 69.2%, 11.2% and 4.4%, respectively. All three modes pass the Mont Carlo test at the 10% level.

As shown in FIG. 3a and d, the spatial pattern of the first EOF mode shows a nonuniform warming. The warming rate over land is much higher than over the oceans because of their different heat capacities. Meanwhile, the warming rate over the Indian Ocean, tropical West Pacific and Atlantic around northern Africa and the southern Atlantic is relatively higher than over other oceans, which agrees with previous research (Mccrystall et al. 2021). PC1 agrees well with the GW index in terms of the increasing trend. The correlation coefficient between them is 0.99, although fluctuation of PC1 is visible. That is, the first mode is identified as the GW mode.

As shown in FIG. 3b and e, the second EOF mode, with 11.2% of the variance, can be easily identified as the IPO mode. Meanwhile, the correlation coefficient between PC2 and the IPO index reaches up to 0.88 and is significant at the 1% level. During the positive phase of the IPO, uniform warm anomalies are apparent over the Indian Ocean, central-eastern tropical Pacific and southern Atlantic, whereas cold anomalies exist over the northwestern and southwestern Pacific and northern Atlantic. During the positive phase of the IPO, the terrestrial SAT over eastern and southern North America, South Asia and the land around the Mediterranean become cooler, while the terrestrial SAT over Alaska, western Canada, the Siberian Plain, the Mongolian Plateau, and Australia, is warm.

The third EOF mode, with only 4.4% of the variance (FIG. 3c, f), is recognizable as the AMO, based on the dipole SAT in the northern and southern Atlantic. Meanwhile, the correlation coefficient between PC3 and AMO index is 0.53, and significant at the 5% level. During the positive phase of the AMO, the SAT is warm over northern Lake Baikal, eastern China, western North America, the northern and central Pacific, and northern Atlantic, while cooling occurs over the Indian Ocean and Southern Ocean.

To further investigate the spatial distributions of SAT related to GW, the IPO and the AMO, singular value decomposition (SVD) analysis was applied to the globally terrestrial SAT from CRU and tropical SST (20°S–45°N) from the Hadley Center during the period 1934–2020. Prior to the analysis, we removed the interannual variation by applying a 9-year Lanczos low-pass filter.

The heterogeneous fields of the first three coupled modes and the related time series are shown in FIG. 4. Their variances are 96.0%, 2.6% and 0.5%, respectively. Only the first two modes passed the Mont Carlo test at the 10% level.

For the first coupled mode from the SVD analysis, both FIG. 4a and FIG. 4d show a significant warming trend, except for the SST over the northen Pacific, which somehow differs from the consistent GW

conclusion found in previous studies (Xie et al. 2010; Mohino et al. 2011; Gu and Adler 2015). The implication, therefore, is that this mode is probably mixed with decadal and interdecadal oscillations that the SVD analysis could not completely separate. The correlation coefficient between the GW index and the PC1 of SST reaches up to 0.93, and the PC1 of the terrestrial SAT also reaches a high value, of up to 0.94 (FIG. 4g). A weak downward trend is visible from 1943 to 1970, which may be due to the residual interdecadal SST signals (Dong and Mcphaden 2017b, a) or related to changes in global-mean temperature because of the high concentrations of anthropogenic aerosols during that period (e.g., Wilcox et al. 2013). Unsurprisingly, the first mode is the GW mode and its variance contribution rises from 69.2% based on the EOF analysis to 96.0% based on the SVD analysis.

For the second coupled mode from the SVD analysis, the IPO mode can be identified, based on the postive SSTA in the central-eastern tropical Pacific and negtive SSTA in the Northwest Pacific (FIG. 4b), as well as the corresponding time series (FIG. 4h) being highly correlated (correlation coefficient of 0.93) with the IPO index. Therefore, the SST pattern in the second mode can be identified as the IPO mode. However, the variance contribution of the IPO decreases from 11.2% based on EOF analysis to 2.6% based on SVD analysis. During the positive phase of the IPO, the terrestrial SAT over Alaska, western Canada, Peru, and northern Australia is warm, while the terrestrial SAT over eastern and southern North America, southern Greenland, the northern Indian subcontinent, and the land areas around the Mediterranean become cooler, which is consistent with the EOF analysis. This mode is slightly contaminated by the AMO, which can be seen from the negtive SSTA in the North Atlantic (Chen and Tung 2018). Acording to FIG. 4b, the negative phase of the AMO is embedded in the positive phase of the IPO in some periods, which is also reflected in FIG. 1.

Although the third SVD mode fails to pass the significance test at the 10% level, the SST in the northern Atlantic is characterized by positive anomalies, as shown in FIG. 4c, and the correlation coefficient between the time series of the SST and AMO in FIG. 4i is 0.56, which is statistically significant at the 5% level. Thus, it is believed that the third mode is the AMO. During the positive phase of the AMO, the terrestrial SAT over eastern Europe is cool, while that near the Gulf of Guinea, the high altitudes of the Andes Mountains, and South China become warm where the GW trend is insignificant.

The above results indicate that the low-frequency variability of SAT is closely related to GW, the IPO and the AMO, and GW contributes about 96% of the variance. In the following section, we further investigate the causality via the information flow method (Liang, 2014).

3.2 Causality between GW, the IPO, the AMO, and global SAT

Owing to correlation, EOF or SVD analysis lacking directetness or asymmetry and hence not implying causality, we therefore applied the information flow method to validate the above results and explore the impacts of **GW, the IPO and the AMO** on SAT variation.

FIG. 5a and b show the information flow from GW to the global SAT from CRU during 1934−2020 and from GISS during 1948−2020. The patterns from SSA (FIG. 2e, f) are the same as those from information

flow (FIG. 5a, b). There is high information flow from GW to SAT over the regions of Mexico, the East African Plateau, the Arabian Peninsula, the Mongolian Plateau, the Tibetan Plateau, and the Great Australian Basin, as well as ocean areas such as the nothern Indian Ocean, tropical West Pacific, and some the Atlantic. This is consistent with the percentage variance in the secular trend as shown in Fig. 2e and f. Therefore, it can be verified that the secular trends of SAT across the globe are caused by GW, except in the central North Pacific, central equatorial Pacific, and northern North Atlantic. This mainly stems from the local decadal and multidecadal variation modes of SST, i.e., the IPO and AMO, which is also visible from the SSA results (FIG. 2b, d).

The information flow from the IPO to SAT is depicted in FIG. 5c and d. It is clear that over the tropical Indian, central-eastern tropical Pacific, central North Pacific, central South Pacific, subtropical northeastern Pacific, tropical Atlantic, northwestern North America, and southeastern America, the causality is significant. The spatial pattern of information flow from the IPO to SAT is similar to the effect of El Niño-Southern Oscillation (ENSO). This is because the IPO index contains high interannual varaibility of ENSO (Chen and Tung 2018), which should not be removed as requested by the algorithm of the information flow method.

FIG. 5e and f display the information flow from the AMO to SAT. Significant causality can be detected over the northwestern Pacific and southwestern Pacific besides the North Atlantic, which is consistent with the findings of Sun et al. (2017), who suggested that the SST varaiblity over the western tropical Pacific can largely be explained by the AMO. Wu et al. (2022) demonstrated that the SST varaiblity over the western tropical Pacific is controlled by the AMO through the variability of the subtropical mode water. This is verified in the present study via infromation flow and further suggests that the SAT not only over the northwestern Pacific but also over the southwestern Pacific can be explained by the AMO, rather than the IPO. Significant causality from AMO to SAT over southern North America and eastern Australia are also detected, as shown both in Fig. 5e and f. However, the significant causality over Brazil, Greenland, Africa, South Asia, the Arabian peninsula are only detected in CRU as shown Fig. 5e, but the signal disappears in GISS because of the locally missing data (Fig. 5f).

4 Precipitation

4.1 Decadal variability, multidecadal variability, and secular trend of global precipitation

Although Tao et al. (2021) investigated the the relative contributions of GW, the IPO and the AMO to the terrestrial precipitation variabilities during 1934–2015, they did not present the distribitions of the significant decadal, multidecadal and secular variabilities across the globe. In this section, we present these and focus particularly on the change in terrestrial precipitation in EAMH, where the secular trend is notable but relatively few studies have discussed it. The related circulation change is examined using the results from the artificial neutral networks with the SOM.

FIG. 6–8 show the distributions of percentage variance in the decadal, multidecadal and secular bands following the application of SSA to the terrestrial precipitation data from GPCC during 1934–2020. As

can be seen in these figures, the decadal and multidecadal components occupy less areas than secular trend. The contributions of decadal and multidecadal variability are less than 10% of the total variance at most grid points. It should be noted that the color bars in in FIG. 6−8 are different from the one in FIG. 2, and the interannual (2−10-year) variability of precipitation carries the most importance (figure not shown), which is very different from that of SAT.

The significant decadal (10−20-year) variability of terrestrial precipitation does not cover much of the globe (FIG. 6), the notable exceptions being southwestern America, northern Canada, the Amazon in South America, South Africa, and northwestern India, east to the Caspian Sea and eastern Australia. The significant multidecadal (20−50-year) variability of terrestrial precipitation is identified in northeastern North America, northwestern South America, the Niger River in Mali, the Congo Basin, Mongolian Plateau, and northern Siberia Plain, north to the Kamchatka Peninsula and central Australia (FIG. 7).

As shown in FIG. 8, the extremely low-frequency (>50-year) variability is significant across the Sahel, the high latitudes of Euraisa, the Tibetan Plateau, western Australia, the areas around Hudson Bay, and southern America. By comparing FIG. 8 and FIG. 2, we conclude that terrestrial precipitation does not follow the "warmer-gets-wetter" pattern, with the Tibetan Plateau being the only exception. The secular trends of precipitation are especially prominent in the high latitudes of Euraisa, from which several important questions emerge: Is there an increase or decrease since 1934? In which season does the trend occur? Is it related to circulation change? These questions are investigated in the next section. Considering the circulation affecting on precicpitation differs from season to season, we explored these questions in the boreal summer half-year (May−October) and boreal winter half-year (November−April), separately.

4.2 Dominant SST modes and causality related to the low-frequency variability of May−October precipitation in EAMH

In this section, we focus on the cause of the secular trends in May−October precipitation in EAMH, which has lacked attention until now.

We begin by examining the spatial distributions of precipitation in EAMH (25°−76°N, 13°W−189°E) and the coupling with SST in the tropics (20°S−45°N) during 1934−2020 by analyzing the SVD analysis results. Before the analysis, the interannual variations of precipitation and SST were removed via a 9-year Lanczos low-pass filter.

The heterogeneous fields of the first three coupled modes and the related time series in May−October are shown in FIG. 9. Their variances are 71.2%, 12.4% and 3.9%, respectively. All three modes passed the Monte Carlo test at the 10% level.

In the summer half-year, the first coupled mode of SST is identifiable as the GW mode, based on the SSTA pattern featuring a positive SSTA covering most of the tropical oceans, especially the tropcial Indian Ocean, western Pacific and Atlantic (FIG. 9a), and the prominent upward trend of the time series (FIG. 9g).

The time series of both SST and precipitation are highly correlated with the GW index, with correlation coefficients reaching 0.94. Surprisingly, the variance contribution of GW is very high, at up to 71.2%. The related precipitation increases with GW over most regions, especially the Scandinavian Peninsula, east to the Ural Mountains, eastern Siberia, the Tibetan Plateau and Xinjiang of China.

For the second coupled mode from the SVD analysis, the IPO mode can be identified, based on the postive SSTA in the central-eastern tropical Pacific and negtive SSTA in the Northwest Pacific (FIG. 9b), as well as the corresponding SST time series (FIG. 9h) being highly correlated with the IPO index (correlation coefficient: 0.89). The variance contribution from the IPO is 12.4%, which is far less than the variance contribution from GW. As shown in FIG. 9e, the related precipitation shows a "dry in the northeast and wet in the southwest" pattern in EAMH during the IPO's positive phase. In particular, the land areas around the Volga River, the Altai Mountains, and east to Lake Baikal become wet while the land over the West Siberian Plain become dry during the IPO's positive phase.

Although the third SVD mode passes the significance test at the 10% level, the SST in most of the northern Atlantic is characterized by positive anomalies, as shown in FIG. 9c, but the correlation coefficient between the time series of SST and the AMO is nonsignificant (FIG. 9i). Thus, the third mode cannot be recognized as the AMO and does not need to be discussed any further.

As mentioned in section 3, correlation, EOF or SVD analysis lacks directetness or asymmetry and hence does not imply causality, leading us to apply the information flow method to further validate the results of section 4.2.

FIG. 10a–c show the information flow from GW, the IPO and the AMO to the May–October precipitation in EAMH during 1934–2020, respectively. It is clear that the information flow map from GW to pecicpitation (FIG. 10a) is highly similar to the precipitation map of the first SVD mode (FIG. 9d). That is, the wet trend over the Scandinavian Peninsula, east to the Ural Mountains, eastern Siberia, the Tibetan Plateau and Xinjiang of China, is caused by GW. The IPO is the second largest contributor according to the SVD analysis; however, there is little information flow from the IPO to the May–October precipitation in EAMH (FIG. 10b). Consequently, the IPO cannot be attributed to the variarion in May–October precipitation in EAMH. Nonetheless, even if the AMO is not an important factor according to the SVD analysis, it does affect the precipitation north of the Caspian Sea, south of Lake Balkhash, and over the Tibetan Plateau and central and eastern Siberia, according to the information flow analysis (FIG. 10c).

So far, we have identified that GW is the dominant factor for the increase in precipitation in EAMH. Therefore, we next applied the SOM approach to uncover the synoptic circulation change related to GW for further exploring the mechanism of the wet trend in EAMH.

Compared with the wind field, the precipitation anomaly can be described more directly from the perspective of water vapor transport. Besides, water vapor convergence (or divergence) has a significant effect on precipitation (Starr et al. 1958; Chen and Tzeng 1990; Bosilovich et al. 2015). In short, the vertically integrated water vapor transport can reflect both the evolution of low-level circulation and the

distribution of the water vapor budget. Accordingly, global (56°S−76°N) daily vertically integrated water vapor flux data were used in this study to explore the synoptic circulation change related to GW.

With the vertically integrated water vapor flux inputs, the SOM produces a organized map containing 20 representative nodes in total. Each node represents a key pattern of synoptic circulation and the related time series represents the synoptic circulation frequency anomaly. We calculated the linear trend of each node's time series to find the synoptic pattern that occurs more and more frequently or less and less frequently against the background of GW. It should be noted that for convenience of analysis only the circulation in EAMH is displayed.

FIG. 11 shows the D5 and A4 patterns from the SOM and the related time series, which represent the more and more frequent and less and less frequent synoptic circulation against the background of GW, respectively. As shown in FIG. 11c, a strong cyclone covers northern Europe, with westerly transports of water vapor from the northeastern Atlantic to the Eastern European Plain. Meawhile, there are easterly transports of water vapor from the northwestern Pacific to eastern Siberia. These synopitc circulations are favorable for precipitation in EAMH, especially over northern Europe and eastern Siberia. The trend of the synoptic circulation frequency is 0.11 during 1950−2020, which is significant at the 10% level. On the other hand, the synoptic circulation as shown in FIG. 11d occurs less and less and its significant trend at the 10% level is −0.26 during 1950−2020 (FIG. 11b). The synoptic circulation in FIG. 11d is almost the opposite of that in FIG. 11c: an anticyclone covers northern Europe and northeastern Atlantic, with easterly water vapor transport. Meanwhile, there is a branch of water vapor outflow from eastern Siberia to the northwestern Pacific. Therefore, synopitc circulations are unfavorable for precipitation in EAMH.

The intensified westerly water vapor transport at 50°N and weakened East Asian summer monsoon in the last 70 years, as shown in FIG. 11a and c, are consistent with the findings of previous studies (Wang 2001; Huang et al. 2004; Ding et al. 2008; Yang et al. 2020; Kanamori et al. 2023).

4.3 Dominant SST modes and causality related to the low-frequency variability of November−April precipitation in EAMH

In this section, the same procedures are applied to the November−April precipitation in EAMH to investigate the cause of the wet trend **in** this region.

FIG. 12 shows the first three coupled modes from SVD for the November−April precipitation in EAMH and the tropical SST. Their variances are 72.9%, 11.3% and 5.6%, respectively. All three modes passed the Monte Carlo test at the 10% level.

It is apparent that in the winter half-year the first coupled mode of SST is also the GW mode, based on the SSTA pattern featuring a positive SSTA covering most of the tropical oceans, especially the tropcial Indian Ocean, western Pacific and Atlantic (FIG. 12a), and the prominent upward trend of the time series of SST and precipitation (FIG. 12g). Both time series are highly correlated with the GW index, with correlation coefficients reaching 0.93. The variance contribution of GW reaches up to 72.9%. The related

precipitation increases significantly with GW from western Europe north of 50°N to central Siberia Plain as well as the Tibetan Plateau (FIG. 12d). Meanwhile, the land areas around the Mediterranean Sea become dry.

The second coupled mode from the SVD analysis is also identifiable as the IPO mode, based on the SSTA pattern (FIG. 12b) and the corresponding SST time series (FIG. 12h) being highly correlated with the IPO index (correlation coefficient: 0.89). The variance contribution from the IPO is only 11.3%. During the IPO's postive phase, wet anomalies can be seen over central Siberia and dry anomalies over eastern Sibeira, Mongolia and North China. For the third mode, the correlation coefficient between the time series of SST and the AMO is nonsignificant (FIG. 12i). Thus, the third mode cannot be recognized as the AMO and does not need to be discussed any further.

The information flow from GW, the IPO and the AMO to the November–April precipitation during 1934–2020 is shown in FIG. 13. The causality pattern (FIG. 13a) is similar to the wet trend pattern (FIG. 12d). That is, the increased precipitation in November–April over the East European Plain, West Siberian Plain, Central Siberian Plateau, and Tibetan Plateau can be explained by GW. Significant causality from the IPO to precipitation (FIG. 13b) can be detected from the area north of the Black Sea to the northeast of Lake Balkhash. For the AMO (FIG. 13c), it is the cause of precipitation over northern Siberia and northwestern and northeastern China.

FIG. 14 shows the synoptic circulation of vertically integrated water flux from the SOM and the related time series, which have a significant trend against the background of GW. As shown in FIG. 14a and c, the synoptic circulation related to the significant increasing wet trend in the winter half-year is characterized by a strong anticyclone covering the Mediterranean. Meanwhile, there is an elongated cyclone covering northern Europe and the West Siberian Plain with westerly flow between them transporting water vapor from the northeastern Atlantic to the Eastern European Plain and West Siberian Plain, causing water vapor convergence over central Siberian Plateau. The synoptic circulations are favorable for precipitation in the East European Plain, West Siberian Plain, and central Siberian Plateau. The trend of the synoptic circulation frequency is 0.17 during 1950–2020, which is significant at the 10% level.

On the other hand, the synoptic circulation in the winter half-year, as shown in FIG. 14d, occur less and less, with a −0.14 trend, during 1950–2020 (FIG. 14b). The synoptic circulations in FIG. 14d are characterized by an anticyclone covering the East European Plain and West Siberian Plain, cyclones covering the Mediterranean Sea and northeastern Atlantic, and easterly flow from Lake Baikal to the northeastern Atlantic, which are unfavorable for precipitation in EAMH.

5 Summary

Based on the SSA method, this paper presents the relative magnitudes of the decadal (10–20-year), multidecadal (20–50-year) and secular (>50-year) components of global SAT and terrestrial precipitation over EAMH during 1934–2020. Then, SVD analysis was applied to identify the SST modes (GW, the IPO and the AMO) that have the significant effects on the low-frequency variabilities of SAT and terrestrial

precipitation. Furthermore, we used the information flow method to verify the causality of the SST modes with respect to the SAT and terrestrial precipitation. Finally, artificial neural networks with an SOM were further applied to reveal the synoptic circulation changes from GW that can explain the secular wet trend over EAMH. The results of the study can be summarized as follows:

1. GW is the first dominant causal factor for SAT. The SAT mainly shows a unified secular trend globally across both land and ocean. In particular, the variance of the secular trend over the Indian Ocean, tropical West Pacific and Atlantic, as well as over land areas such as Mexico, the East African Plateau, the Arabian Peninsula, Mongolian Plateau, Tibetan Plateau and the Great Australian Basin, accounts for up to 70%.

2. Although the warming rate over land is much greater than that over the oceans owing to their different heat capacities (which is visible from the EOF results in FIG. 3), the relative magnitudes of the secular trends over the Indian Ocean and tropical West Pacific are higher than those over most land areas (which is a visible from the SSA results in FIG. 2 and the information flow results in FIG. 5). The relative magnitude of the secular trend is small in the central North Pacific, central-eastern tropical Pacific, and northern North Atlantic, which mainly stems from the decadal and multidecadal variation modes of SST, i.e., the IPO and AMO.

3. The IPO is the second most dominant causal factor for SAT, which affects the SAT variability over the tropical Indian Ocean, central-eastern tropical Pacific, central North Pacific, central South Pacific, subtropical northeastern Pacific, and tropical Atlantic, as well as over northwestern America and southeastern North America. The AMO is the last dominant causal factor for SAT, which is able to cause the SAT varaibility over the northwestern Pacific and southwestern Pacific besides the North Atlantic.

4. GW is the first dominant causal factor for the terrestrial precipitation varailiblity in EAMH. A large area with a wet trend can be identified in this region. Moreover, the area with the wet trend in the boreal winter half-year is much larger than that in the boreal summer half-year. The synopitic circulation related to the wet trend is characterized by westerly flow that transports water vapor from the northeastern Atlantic to Eurasia, which is favorable for precipitation there. The IPO is the second dominant causal factor for the terrestrial precipitation varailiblity in EAMH. Howover, its effect could not be cross-validated on the basis of the SVD analysis and information flow results.

Declarations

Data availability The monthly terrestrial SAT data from CRU is available at https://data.ceda.ac.uk/badc/cru/data/cru_ts; The monthly SAT data covering land and ocean from GISS is available at https://data.giss.nasa.gov/gistemp/; The monthly terrestrial precipitation data from GPCC is available at https://opendata.dwd.de/climate_environment/GPCC/html; The daily reanalysis data from

ERA5 is available at https://www.ecmwf.int/en/forecasts/datasets/reanalysis-datasets/era5; The monthly SST data from Met Office Hardley Center is available at https://www.metoffice.gov.uk/hadobs/hadisst/; The IPO and AMO monthly time series data is available at https://psl.noaa.gov/data/climateindices/list/.

Conflict of interest The authors declare having no competing interests.

Consent for publication All authors manifested their consent for publication.

References

1. Allen MR, Ingram WJ (2002) Constraints on future changes in climate and the hydrologic cycle. Nature 419:228-232. https://doi.org/10.1038/nature01092

2. Ault TR, St. George S (2010) The magnitude of decadal and multidecadal variability in north american precipitation. Journal of Climate 23:842-850. https://doi.org/10.1175/2009jcli3013.1

3. Bintanja R, Selten F (2014) Future increases in arctic precipitation linked to local evaporation and sea-ice retreat. Nature 509:479-482. https://doi.org/10.1038/nature13259

4. Bintanja R, Andry O (2017) Towards a rain-dominated arctic. Nature Climate Change 7:263-267. https://doi.org/10.1038/nclimate3240

5. Bosilovich MG, Chern J-D, Mocko D et al (2015) Evaluating observation influence on regional water budgets in reanalyses. Journal of Climate 28:3631-3649. https://doi.org/10.1175/jcli-d-14-00623.1

6. Chen TC, Tzeng RY (1990) Global-scale intraseasonal and annual variation of divergent water-vapor flux. Meteorology and Atmospheric Physics 44:133-151. https://doi.org/10.1007/BF01026815

7. Chen X, Tung K-K (2014) Varying planetary heat sink led to global-warming slowdown and acceleration. Science 345:897-903. https://doi.org/10.1126/science.1254937

8. Chen X, Wallace JM (2015) Enso-like variability: 1900–2013. Journal of Climate 28:9623-9641. https://doi.org/10.1175/jcli-d-15-0322.1

9. Chen X, Tung K-K (2018) Global-mean surface temperature variability: Space–time perspective from rotated eofs. Climate Dynamics 51:1719-1732. https://doi.org/10.1007/s00382-017-3979-0

10. Deser C, Phillips AS, Hurrell JW (2004) Pacific interdecadal climate variability: Linkages between the tropics and the north pacific during boreal winter since 1900. Journal of Climate 17:3109-3124. https://doi.org/10.1175/1520-0442(2004)017<3109:Picvlb>2.0.Co;2

11. Ding Y, Wang Z, Sun Y (2008) Inter-decadal variation of the summer precipitation in east china and its association with decreasing asian summer monsoon. Part i: Observed evidences. International Journal of Climatology 28:1139-1161. https://doi.org/10.1002/joc.1615

12. Dong L, McPhaden MJ (2017a) The role of external forcing and internal variability in regulating global mean surface temperatures on decadal timescales. Environmental Research Letters 12:034011. https://doi.org/10.1088/1748-9326/aa5dd8

13. Dong L, McPhaden MJ (2017b) Why has the relationship between indian and pacific ocean decadal variability changed in recent decades? Journal of Climate 30:1971-1983. https://doi.org/10.1175/JCLI-D-16-0313.1

14. Du J, Tao L, Xu C (2022) Interdecadal variation of land precipitation in china and relative contributions of global warming ipo and amo. Acta Meteorologica Sinica 80:685-700. https://doi.org/10.11676/qxxb2022.055

15. Greve P, Orlowsky B, Mueller B et al (2014) Global assessment of trends in wetting and drying over land. Nature Geoscience 7:716-721. https://doi.org/10.1038/ngeo2247

16. Gu G, Adler RF (2013) Interdecadal variability/long-term changes in global precipitation patterns during the past three decades: Global warming and/or pacific decadal variability? Climate Dynamics 40:3009-3022. https://doi.org/10.1007/s00382-012-1443-8

17. Gu G, Adler RF (2015) Spatial patterns of global precipitation change and variability during 1901–2010. Journal of Climate 28:4431-4453. https://doi.org/10.1175/JCLI-D-14-00201.1

18. Gu G, Adler RF, Huffman GJ et al (2007) Tropical rainfall variability on interannual-to-interdecadal and longer time scales derived from the gpcp monthly product. Journal of Climate 20:4033-4046. https://doi.org/10.1175/JCLI4227.1

19. Hansen J, Ruedy R, Sato M et al (2010) Global surface temperature change. Reviews of Geophysics 48. https://doi.org/10.1029/2010RG000345

20. Harris I, Osborn TJ, Jones P et al (2020) Version 4 of the cru ts monthly high-resolution gridded multivariate climate dataset. Scientific Data 7:109. https://doi.org/10.1038/s41597-020-0453-3

21. Held IM, Soden BJ (2006) Robust responses of the hydrological cycle to global warming. Journal of Climate 19:5686-5699. https://doi.org/10.1175/JCLI3990.1

22. Held IM, Delworth TL, Lu J et al (2005) Simulation of sahel drought in the 20th and 21st centuries. Proceedings of the National Academy of Sciences 102:17891-17896. https://doi.org/10.1073/pnas.0509057102

23. Hersbach H, Bell B, Berrisford P et al (2020) The era5 global reanalysis. Quarterly Journal of the Royal Meteorological Society 146:1999-2049. https://doi.org/10.1002/qj.3803

24. Hewitson BC, Crane RG (2002) Self-organizing maps: Applications to synoptic climatology. Climate Research 22:13-26. https://doi.org/10.3354/cr022013

25. Huang R, Huang G, Wei Z (2004) Climate variations of the summer monsoon over china. East asian monsoon, WORLD SCIENTIFIC, pp 213-268

26. IPCC (2007) Climate change 2007: The physical science basis. Contribution of working group i to the fourth assessment report of the intergovernmental panel on climate change. Cambridge University Press, Cambridge, United Kingdom and New York, NY, USA

27. John VO, Allan RP, Soden BJ (2009) How robust are observed and simulated precipitation responses to tropical ocean warming? Geophysical Research Letters 36. https://doi.org/10.1029/2009GL038276

28. Kanamori H, Abe M, Fujinami H et al (2023) Impacts of global warming on summer precipitation trend over northeastern eurasia during 1990–2010 using large-ensemble experiments. International Journal of Climatology 43:615-631. https://doi.org/10.1002/joc.7798

29. Kerr RA (2000) A north atlantic climate pacemaker for the centuries. Science 288:1984-1985. https://doi.org/10.1126/science.288.5473.1984

30. Knight JR, Allan RJ, Folland CK et al (2005) A signature of persistent natural thermohaline circulation cycles in observed climate. Geophysical Research Letters 32. https://doi.org/10.1029/2005GL024233

31. Kohonen T (1982) Self-organized formation of topologically correct feature maps. Biological Cybernetics 43:59-69. https://doi.org/10.1007/BF00337288

32. Kosaka Y, Xie S-P (2013) Recent global-warming hiatus tied to equatorial pacific surface cooling. Nature 501:403-407. https://doi.org/10.1038/nature12534

33. Kushnir Y (1994) Interdecadal variations in north atlantic sea surface temperature and associated atmospheric conditions. Journal of Climate 7:141-157. https://doi.org/10.1175/1520-0442(1994)007<0141:Ivinas>2.0.Co;2

34. Li H, Dai A, Zhou T et al (2010) Responses of east asian summer monsoon to historical sst and atmospheric forcing during 1950–2000. Climate Dynamics 34:501-514. https://doi.org/10.1007/s00382-008-0482-7

35. Li M, Jiang Z, Zhou P et al (2020) Projection and possible causes of summer precipitation in eastern china using self-organizing map. Climate Dynamics 54:2815-2830. https://doi.org/10.1007/s00382-020-05150-4

36. Liang XS (2014) Unraveling the cause-effect relation between time series. Physical Review E 90:052150. https://doi.org/10.1103/PhysRevE.90.052150

37. Mantua NJ, Hare SR, Zhang Y et al (1997) A pacific interdecadal climate oscillation with impacts on salmon production. Bulletin of the American Meteorological Society 78:1069-1080. https://doi.org/10.1175/1520-0477(1997)078<1069:Apicow>2.0.Co;2

38. McCabe GJ, Palecki MA, Betancourt JL (2004) Pacific and atlantic ocean influences on multidecadal drought frequency in the united states. Proceedings of the National Academy of Sciences 101:4136-4141. https://doi.org/10.1073/pnas.0306738101

39. McCrystall MR, Stroeve J, Serreze M et al (2021) New climate models reveal faster and larger increases in arctic precipitation than previously projected. Nature Communications 12:6765. https://doi.org/10.1038/s41467-021-27031-y

40. Meehl GA, Hu A, Santer BD et al (2016) Contribution of the interdecadal pacific oscillation to twentieth-century global surface temperature trends. Nature Climate Change 6:1005-1008. https://doi.org/10.1038/nclimate3107

41. Meehl GA, Hu A, Arblaster JM et al (2013) Externally forced and internally generated decadal climate variability associated with the interdecadal pacific oscillation. Journal of Climate 26:7298-7310. https://doi.org/10.1175/jcli-d-12-00548.1

42. Minobe S (1999) Resonance in bidecadal and pentadecadal climate oscillations over the north pacific: Role in climatic regime shifts. Geophysical Research Letters 26:855-858. https://doi.org/10.1029/1999GL900119

43. Mohino E, Janicot S, Bader J (2011) Sahel rainfall and decadal to multi-decadal sea surface temperature variability. Climate Dynamics 37:419-440. https://doi.org/10.1007/s00382-010-0867-2

44. Power S, Casey T, Folland C et al (1999) Inter-decadal modulation of the impact of enso on australia. Climate Dynamics 15:319-324. https://doi.org/10.1007/s003820050284

45. Rayner NA, Parker DE, Horton EB et al (2003) Global analyses of sea surface temperature, sea ice, and night marine air temperature since the late nineteenth century. Journal of Geophysical Research: Atmospheres 108. https://doi.org/10.1029/2002JD002670

46. Schlesinger ME, Ramankutty N (1994) An oscillation in the global climate system of period 65–70 years. Nature 367:723-726. https://doi.org/10.1038/367723a0

47. Schneider U, Hänsel S, Finger PR et al (2022) Gpcc full data monthly product version 2022 at 1.0°: Monthly land-surface precipitation from rain-gauges built on gts-based and historical data. Deutscher Wetterdienst (DWD), Offenbach, Germany. https://doi.org/10.5676/DWD_GPCC/FD_M_V2022_100

48. Screen JA, Simmonds I (2010) The central role of diminishing sea ice in recent arctic temperature amplification. Nature 464:1334-1337. https://doi.org/10.1038/nature09051

49. Serreze MC, Francis JA (2006) The arctic amplification debate. Climatic change 76:241-264. https://doi.org/10.1007/s10584-005-9017-y

50. Sheridan SC, Lee CC (2011) The self-organizing map in synoptic climatological research. Progress in Physical Geography 35:109-119. https://doi.org/10.1177/0309133310397582

51. Starr VP, Peixoto JP, Sons L (1958) On the global balance of water vapor and the hydrology of deserts. Tellus 10:188-194. https://doi.org/10.1111/j.2153-3490.1958.tb02004.x

52. Sun C, Kucharski F, Li J et al (2017) Western tropical pacific multidecadal variability forced by the atlantic multidecadal oscillation. Nature Communications 8:15998. https://doi.org/10.1038/ncomms15998

53. Tao L, Liang XS, Cai L et al (2021) Relative contributions of global warming, amo and ipo to the land precipitation variabilities since 1930s. Climate Dynamics 56:2225-2243. https://doi.org/10.1007/s00382-020-05584-w

54. Vautard R, Ghil M (1989) Singular spectrum analysis in nonlinear dynamics, with applications to paleoclimatic time series. Physica D: Nonlinear Phenomena 35:395-424. https://doi.org/10.1016/0167-2789(89)90077-8

55. Wang H (2001) The weakening of the asian monsoon circulation after the end of 1970's. Advances in Atmospheric Sciences 18:376-386. https://doi.org/10.1007/BF02919316

56. Wei M, Qiao F, Guo Y et al (2019) Quantifying the importance of interannual, interdecadal and multidecadal climate natural variabilities in the modulation of global warming rates. Climate Dynamics 53:6715-6727. https://doi.org/10.1007/s00382-019-04955-2

57. Wilcox LJ, Highwood EJ, Dunstone NJ (2013) The influence of anthropogenic aerosol on multi-decadal variations of historical global climate. Environmental Research Letters 8:024033. https://doi.org/10.1088/1748-9326/8/2/024033

58. Wu B, Xu L, Lin X (2022) Decadal to multidecadal variability of the western north pacific subtropical front and countercurrent. Journal of Geophysical Research: Oceans 127:e2021JC018059. https://doi.org/10.1029/2021JC018059

59. Xie S-P, Deser C, Vecchi GA et al (2010) Global warming pattern formation: Sea surface temperature and rainfall. Journal of Climate 23:966-986. https://doi.org/10.1175/2009JCLI3329.1

60. Xu C, Zhang H, Tao L (2021) Relative contributions of interdecadal pacific oscillation, atlantic multidecadal oscillation and global warming to the land precipitation in north america. Chinese Journal of Atmospheric Sciences (in Chinese) 45:1196-1216. https://doi.org/10.3878/j.issn.1006-9895.2101.20228

61. Yang H, Xu G, Mao H et al (2020) Spatiotemporal variation in precipitation and water vapor transport over central asia in winter and summer under global warming. Frontiers in Earth Science 8. https://doi.org/10.3389/feart.2020.00297

62. Zhang R, Delworth TL (2006) Impact of atlantic multidecadal oscillations on india/sahel rainfall and atlantic hurricanes. Geophysical Research Letters 33. https://doi.org/10.1029/2006GL026267

63. Zhang Y, Wallace JM, Battisti DS (1997) Enso-like interdecadal variability: 1900–93. Journal of Climate 10:1004-1020. https://doi.org/10.1175/1520-0442(1997)010<1004:Eliv>2.0.Co;2

64. Zhao L, Dong W, Dong X et al (2022) Relations of enhanced high-latitude concurrent blockings with recent warm arctic-cold continent patterns. Journal of Geophysical Research: Atmospheres 127. https://doi.org/10.1029/2021jd036117

65. Zhou B, Zhai P, Chen Y (2020) Contribution of changes in synoptic-scale circulation patterns to the past summer precipitation regime shift in eastern china. Geophysical Research Letters 47. https://doi.org/10.1029/2020gl087728

66. Zhou P, Jiang Z (2016) Simulation and evaluation of statistical downscaling of regional daily precipitation over yangtze-huaihe river basin based on self-organizing maps. Climatic and Environmental Research (in Chinese) 21:512-524. https://doi.org/10.3878/j.issn.1006-9585.2016.16097
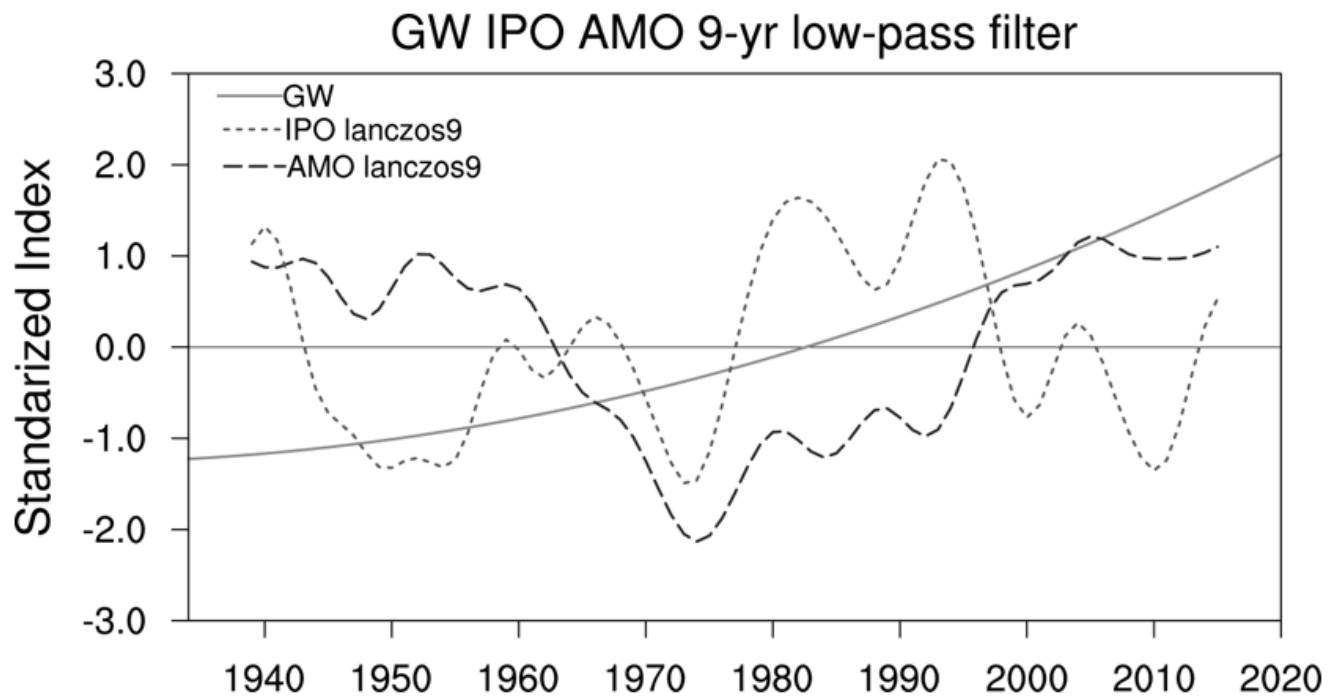
Figures

GW IPO AMO 9-yr low-pass filter

Figure 1

Standardized time series of the GW (solid line) and 9-year low-pass filtered IPO (dotted line) and AMO (dashed line) indexes during 1934–2020.
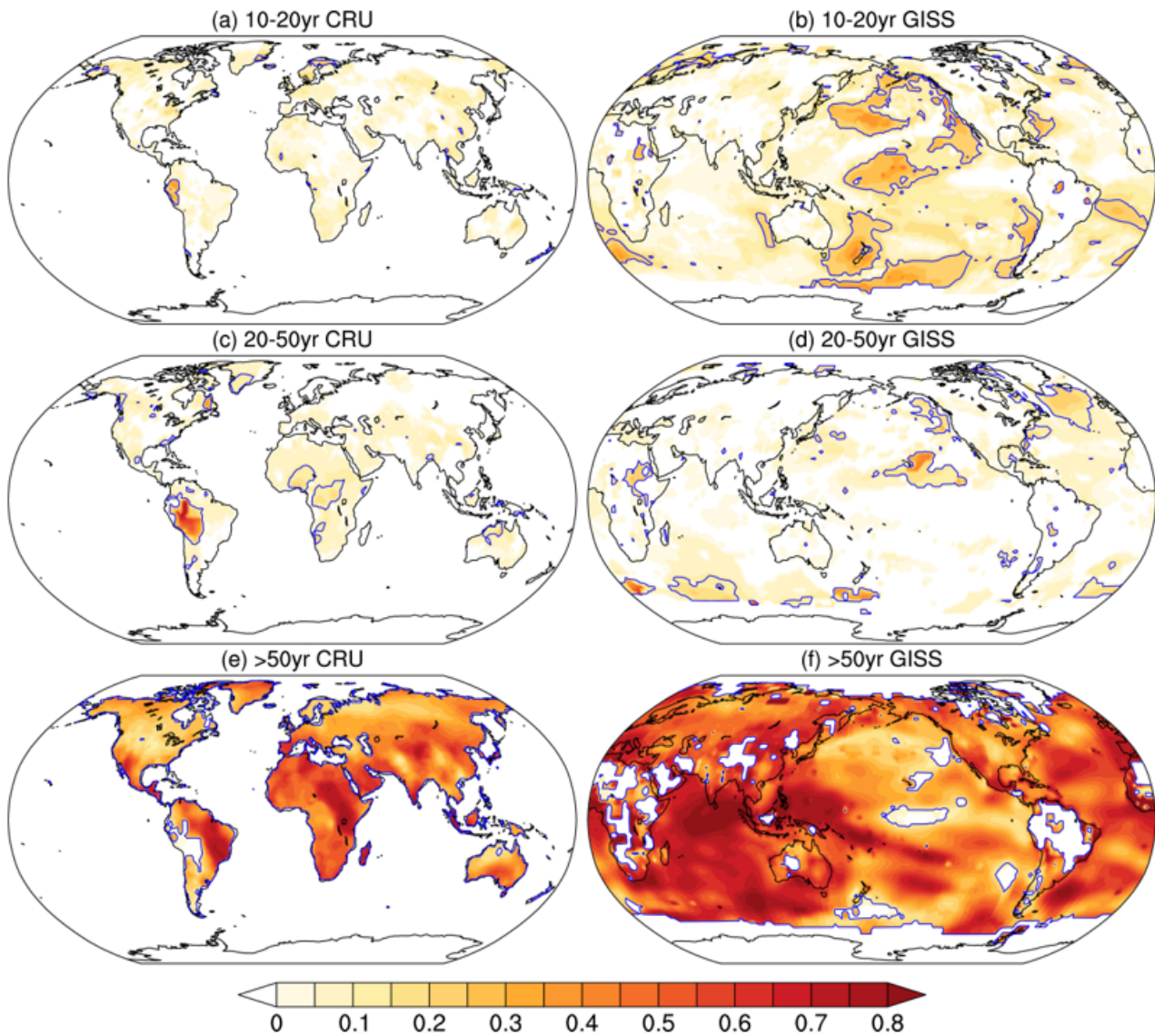
Figure 2

Percentage variance in (a, b) decadal (10−20-year), (c, d) multidecadal (20−50-year) and (e, f) secular (>50-year) bands by applying SSA to SAT from CRU during 1934−2020 (left column) and GISS during 1948−2020 (right column). The blue lines show the regions where the variability in each band is statistically significant at the 10% level according to the Monte Carlo test.
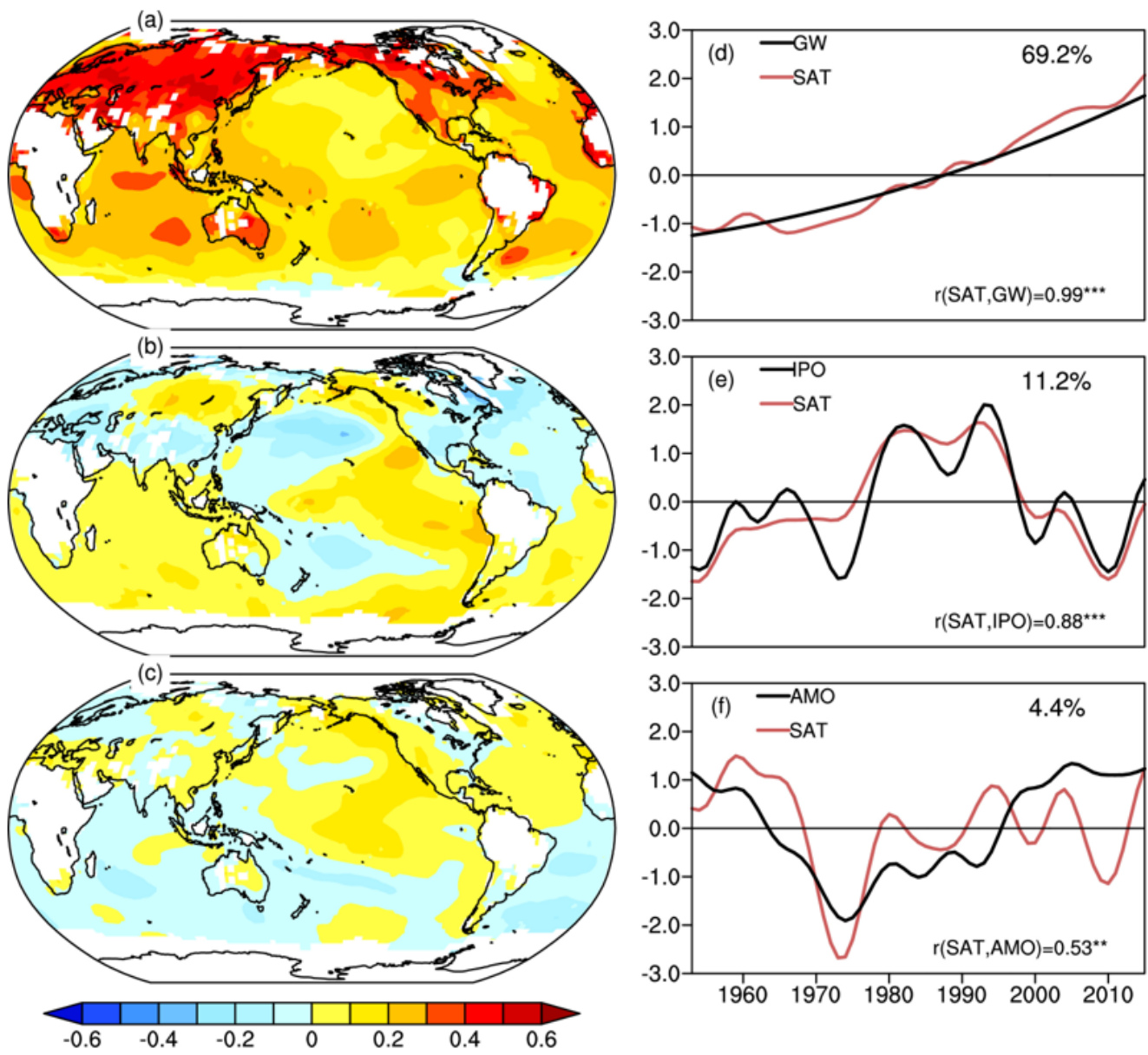
Figure 3

The first three EOF modes of the global SAT from GISS during 1948−2020. Panels (a−c) are the first three spatial patterns of SAT. The normalized EOF time series of SAT (red lines) are shown in (d−f). The black lines in (d−f) are the series of GW, the IPO and the AMO, respectively. The correlation coefficients (r) with *, ** and *** are statistically significant at the 10%, 5% and 1% levels, respectively.
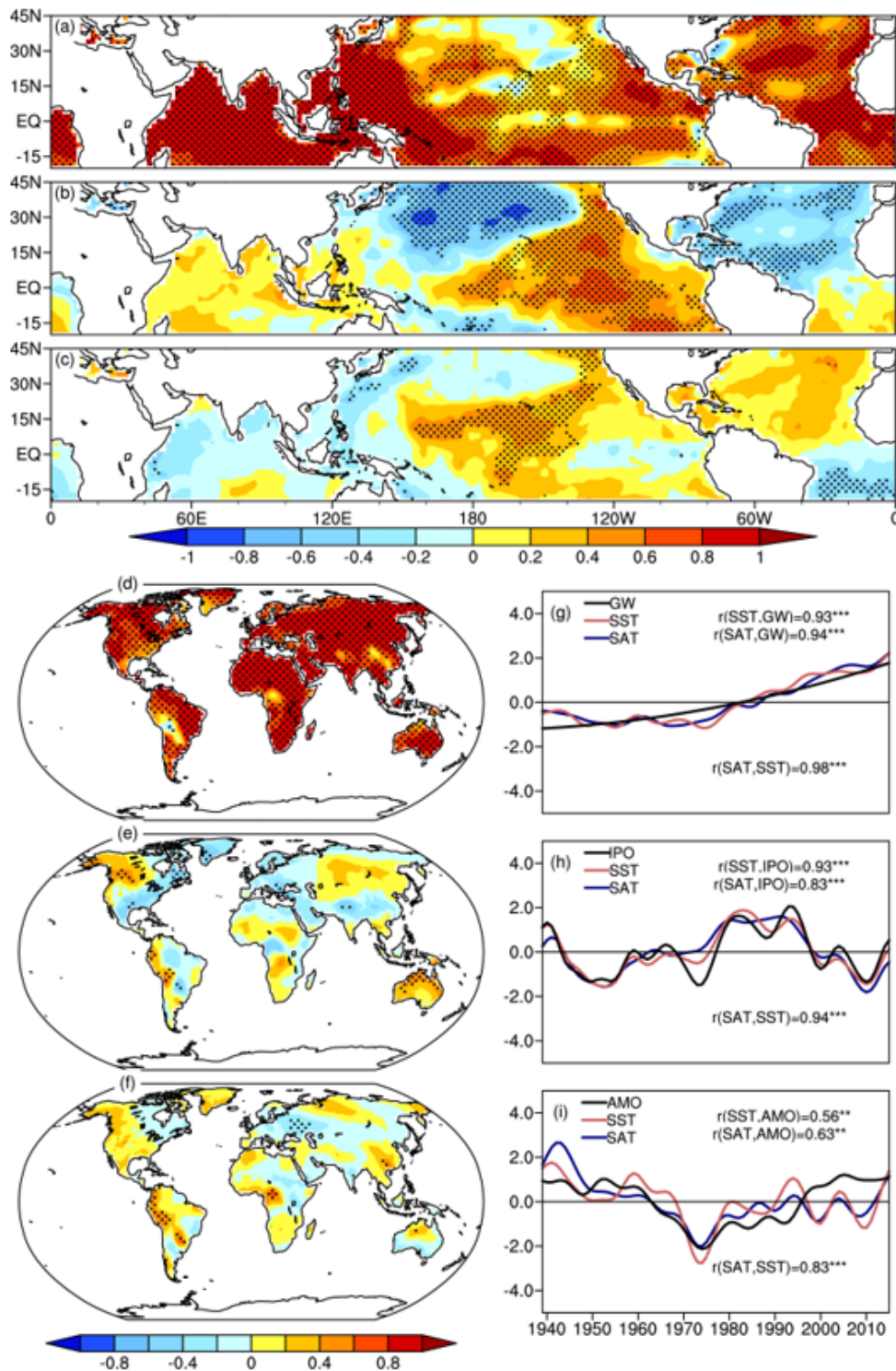
Figure 4

The first three SVD modes between the SST (20S°−45°N) from the Hadley Center and the global terrestrial SAT from CRU during 1934−2020. Panels (a−c) are the first three spatial patterns of SST and panels (d−f) are those of terrestrial SAT. The normalized SVD time series of SST (red lines) and SAT (blue lines) are shown in (g−i). The black lines in (g−i) are the series of GW, the IPO and the AMO, respectively.

The correlation coefficients (r) with *, ** and *** are statistically significant at the 10%, 5% and 1% levels, respectively. The areas with dots are statistically significant at the 10% level.
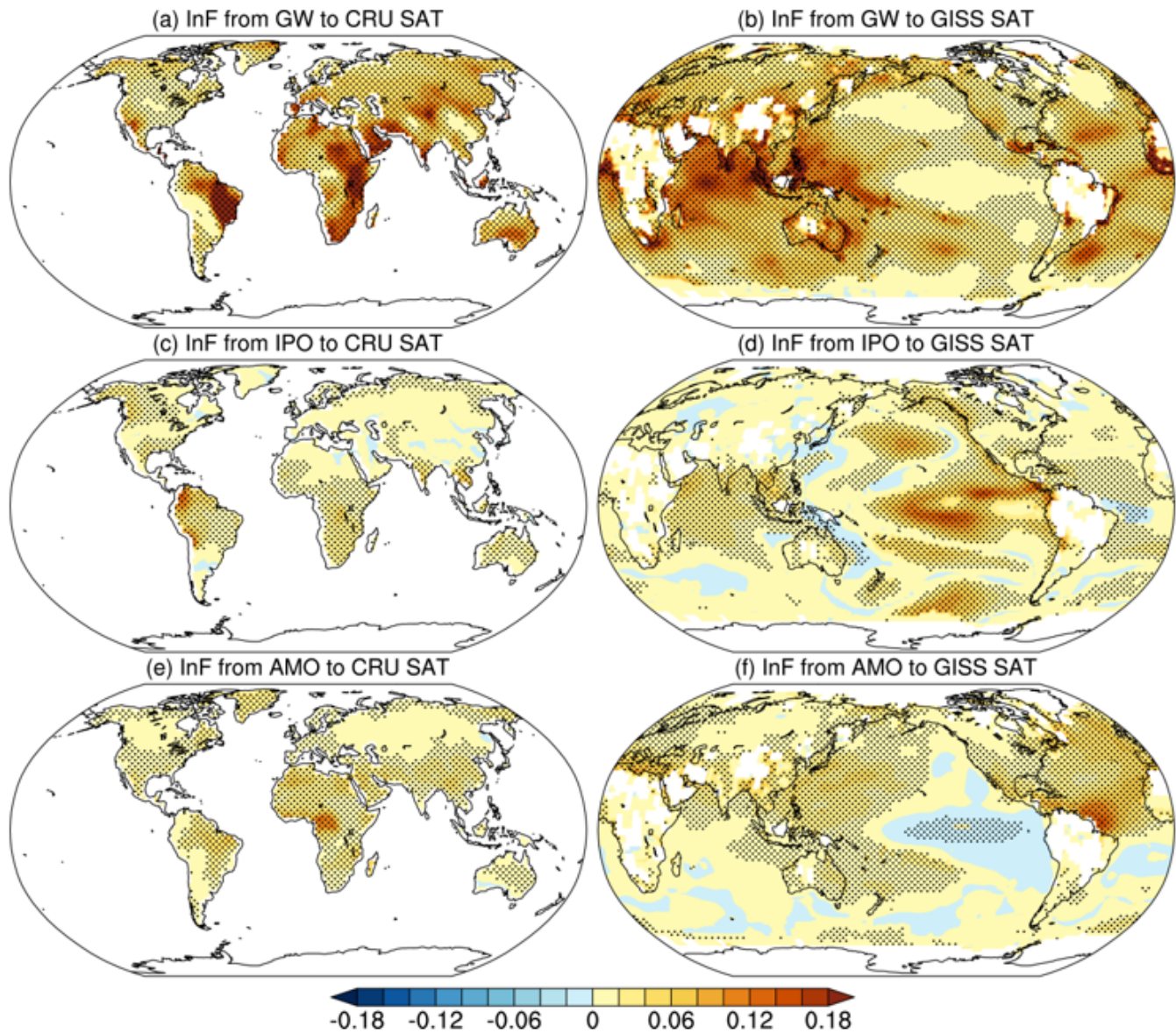
Figure 5

Information flow (nats month^{-1}) from (a, b) GW, (c, d) the IPO, and (e, f) the AMO to SAT from CRU during 1934–2020 (left column) and GISS during 1948–2020 (right column). The areas with dots are statistically significant at the 10% level.
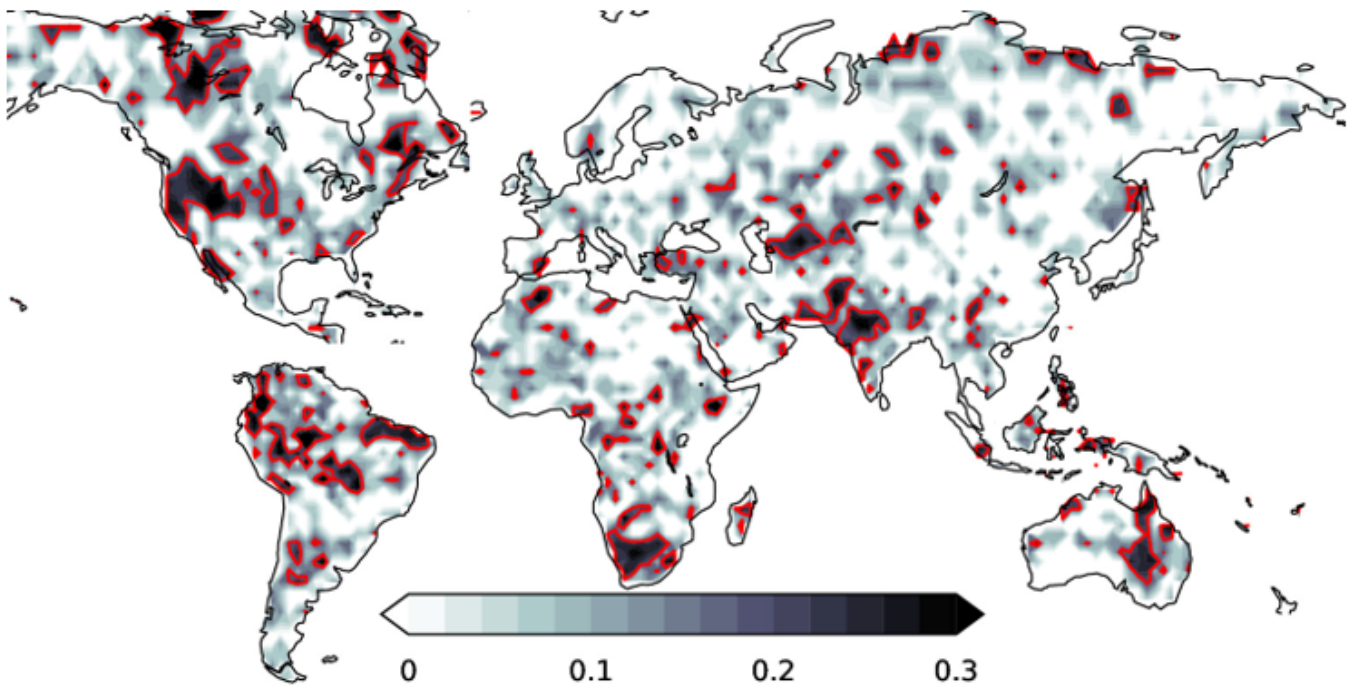
Figure 6

Percentage variance in the decadal (10−20-year) band by applying SSA to terrestrial precipitation from GPCC during 1934−2020. The red lines show the regions where the variability in the decadal band is statistically significant at the 10% level according to the Monte Carlo test.
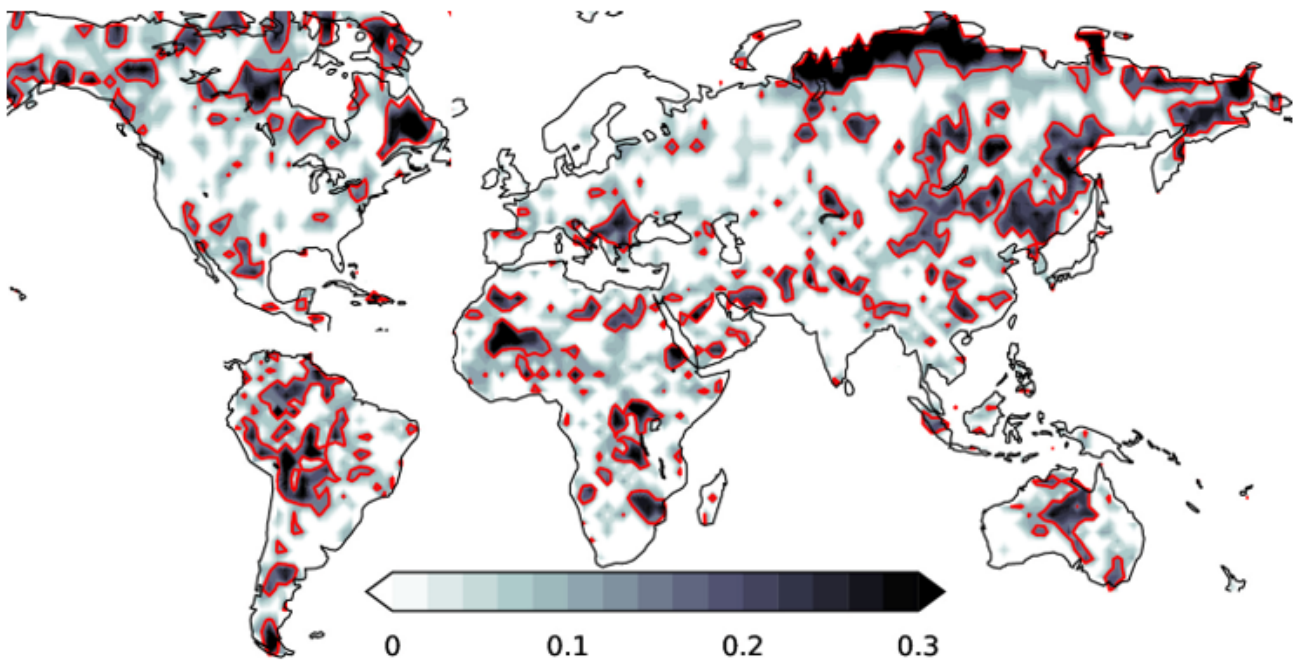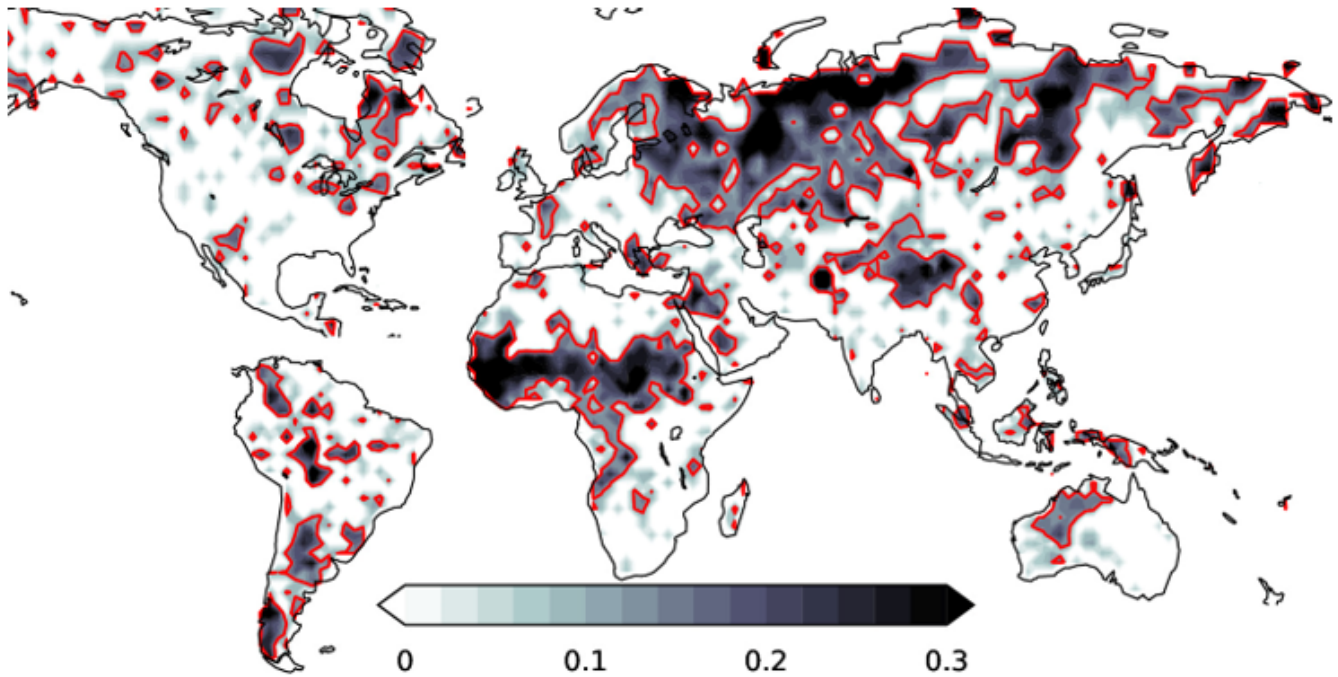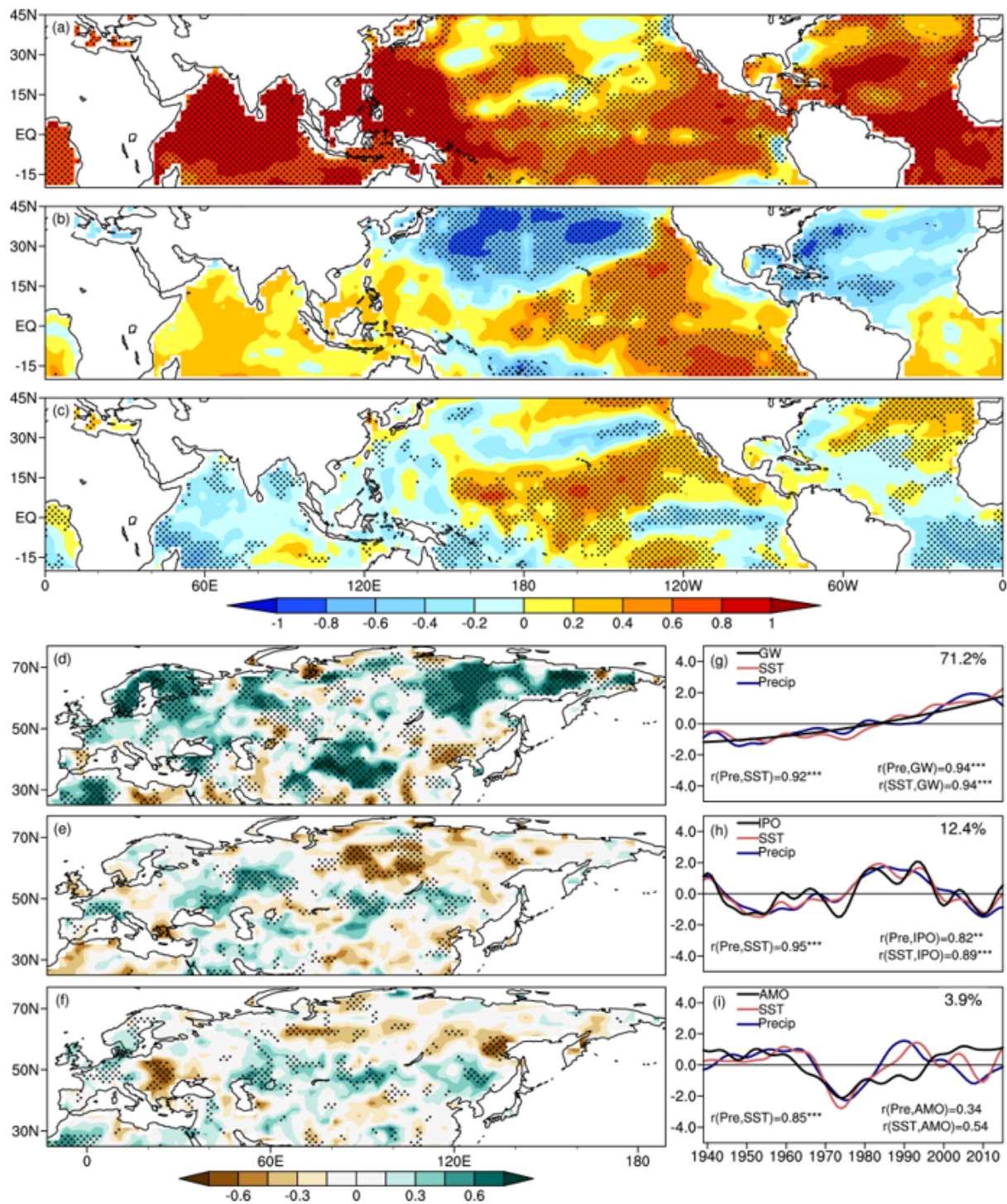
Figure 7

Percentage variance in the multidecadal (20−50-year) band by applying SSA to terrestrial precipitation from GPCC during 1934−2020. The red lines show the regions where the variability in the multidecadal band is statistically significant at the 10% level according to the Monte Carlo test.

Figure 8

Percentage variance in the secular (>50-year) band by applying SSA to terrestrial precipitation from GPCC during 1934−2020. The red lines show the regions where the variability in the secular band is statistically significant at the 10% level according to the Monte Carlo test.

Figure 9

The first three SVD modes between the SST (20°S−45°N) from the Hadley Center and the precipitation (25°−76°N, 13°W−189°E) from GPCC in the summer half-year (May−October) during 1934−2020. Panels (a−c) are the first three spatial patterns of SST and panels (d−f) are those of terrestrial precipitation. The normalized SVD time series of SST (red lines) and SAT (blue lines) are shown in (g−i). The black lines in (g−i) are the series of GW, the IPO and the AMO, respectively. The correlation coefficients (r) with *, ** and

*** are statistically significant at the 10%, 5% and 1% levels, respectively. The areas with dots are statistically significant at the 10% level.
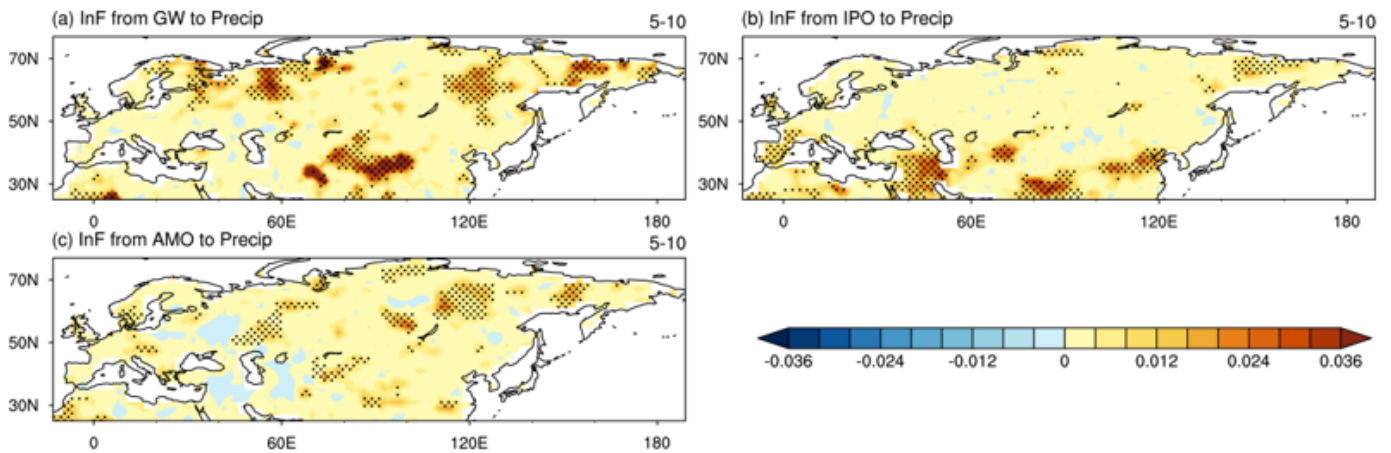
Figure 10

Information flow (nats month^{-1}) from (a) GW, (b) the IPO and (c) the AMO to the terrestrial precipitation from GPCC in the summer half-year (May−October) during 1934−2020. The areas with dots are statistically significant at the 10% level.
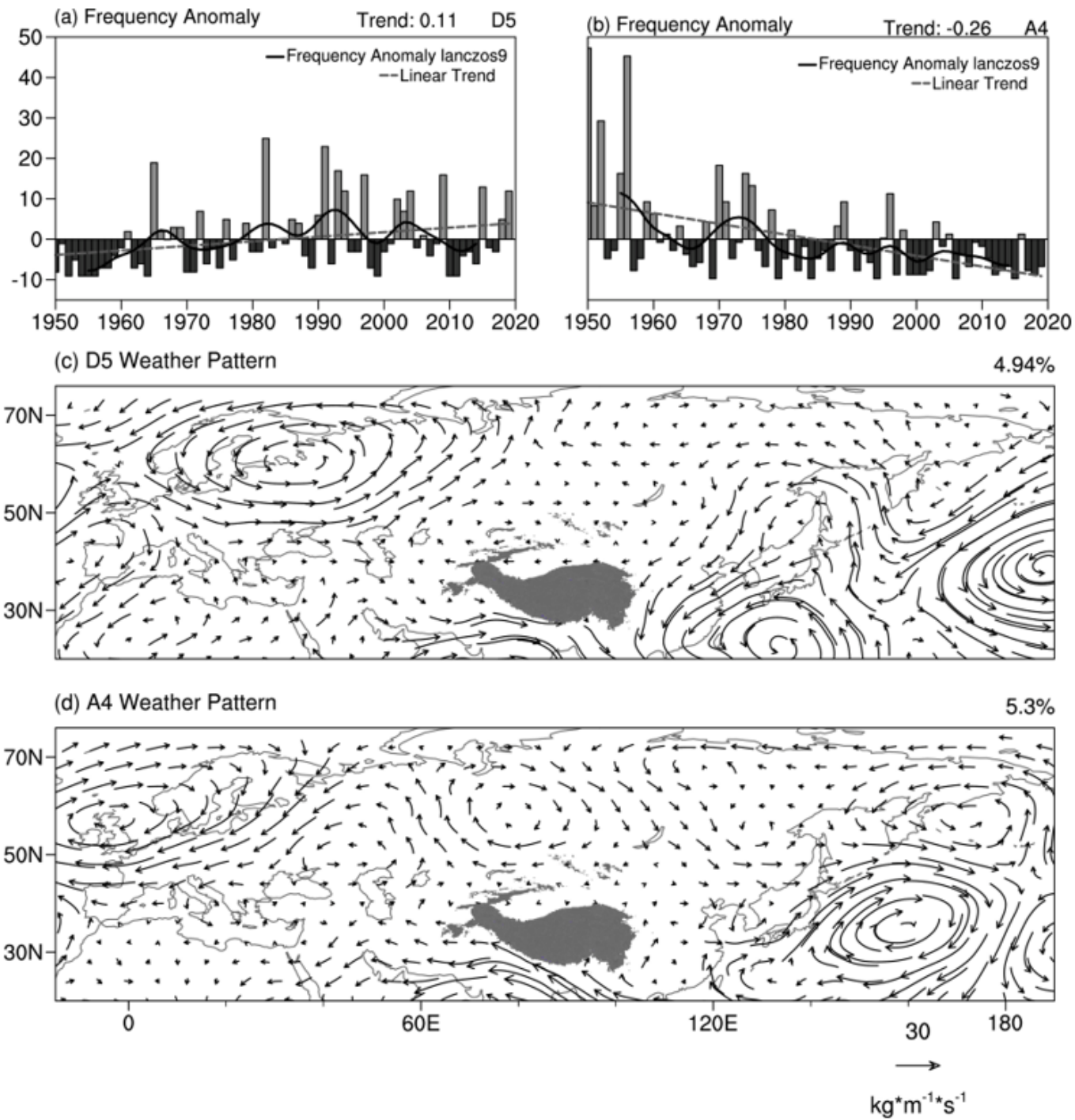
Figure 11

The D5 (c) and A4 (d) patterns (vectors; unit: 30 kg m^{-1} s^{-1}) and their percentage of days (a, b) obtained by the SOM with the global vertically integrated water vapor flux from ERA5 during 1950−2020 in the boreal summer half-year (May−October). The bars in (a, b) are the percentage of days anomalies, the curves are the 9-year low-pass filtered anomalies, and the dashed lines are the trends, which are statistically significant at the 10% level.
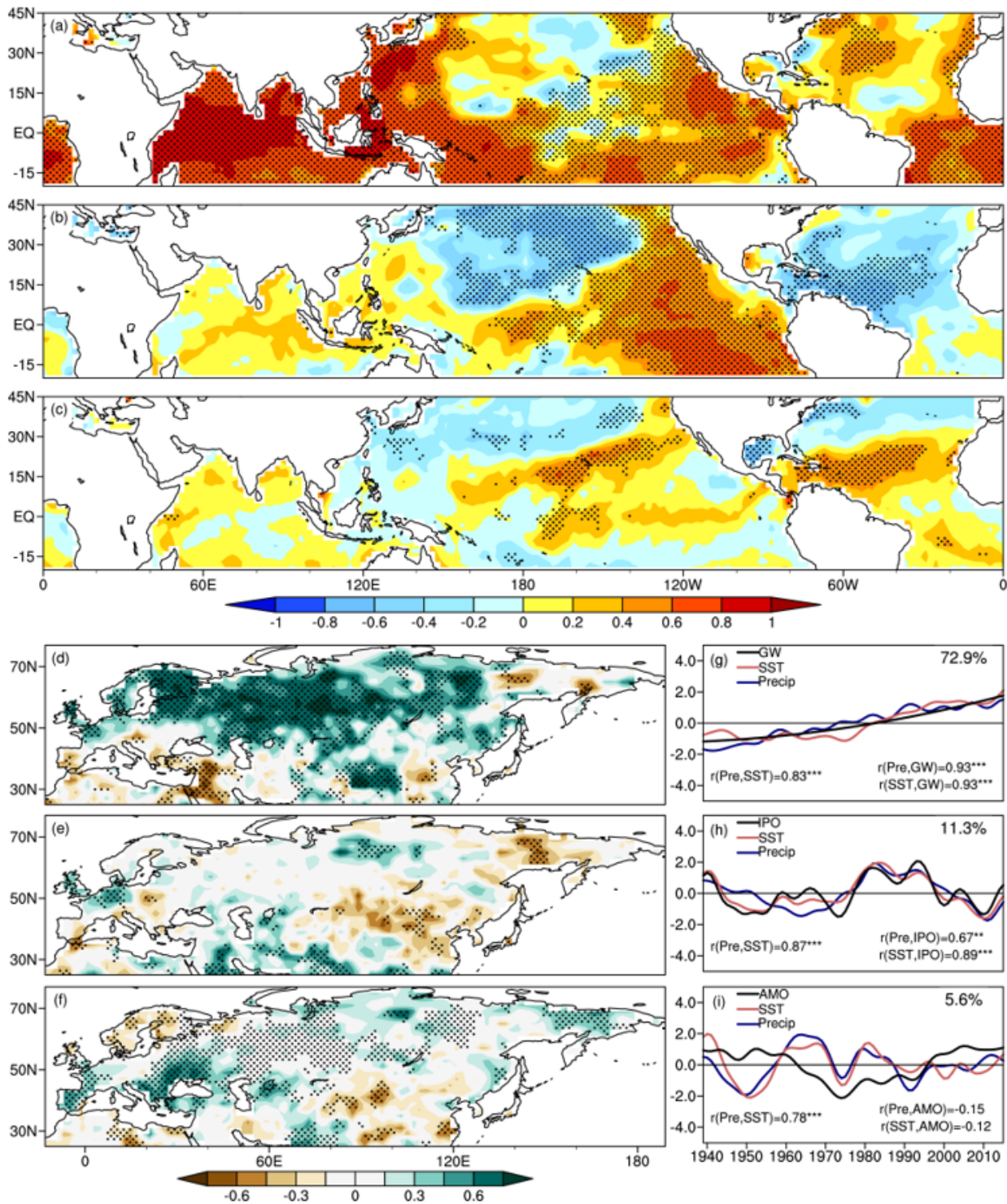
Figure 12

The first three SVD modes between the SST (20°S−45°N) from the Hadley Center and the precipitation over EAMH (25°−76°N, 13°W−189°E) from GPCC in the winter half-year (November−April) during 1934−2020. Panels (a−c) are the first three spatial patterns of SST and panels (d−f) are those of terrestrial precipitation. The normalized SVD time series of SST (red lines) and SAT (blue lines) are shown in (g−i). The black lines in (g−i) are the series of GW, the IPO and the AMO, respectively. The correlation

coefficients (r) with *, ** and *** are statistically significant at the 10%, 5% and 1% levels, respectively. The areas with dots are statistically significant at the 10% level.
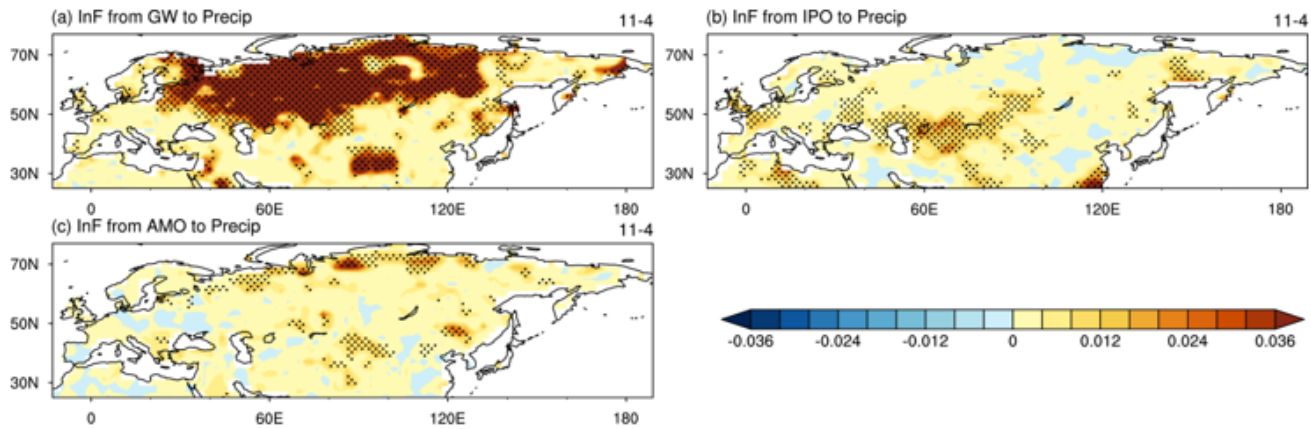

Figure 13

Information flow (nats month^{-1}) from (a) GW, (b) the IPO and (c) the AMO to the terrestrial precipitation from GPCC in the winter half-year (November–April) during 1934–2020. The areas with dots are statistically significant at the 10% level.
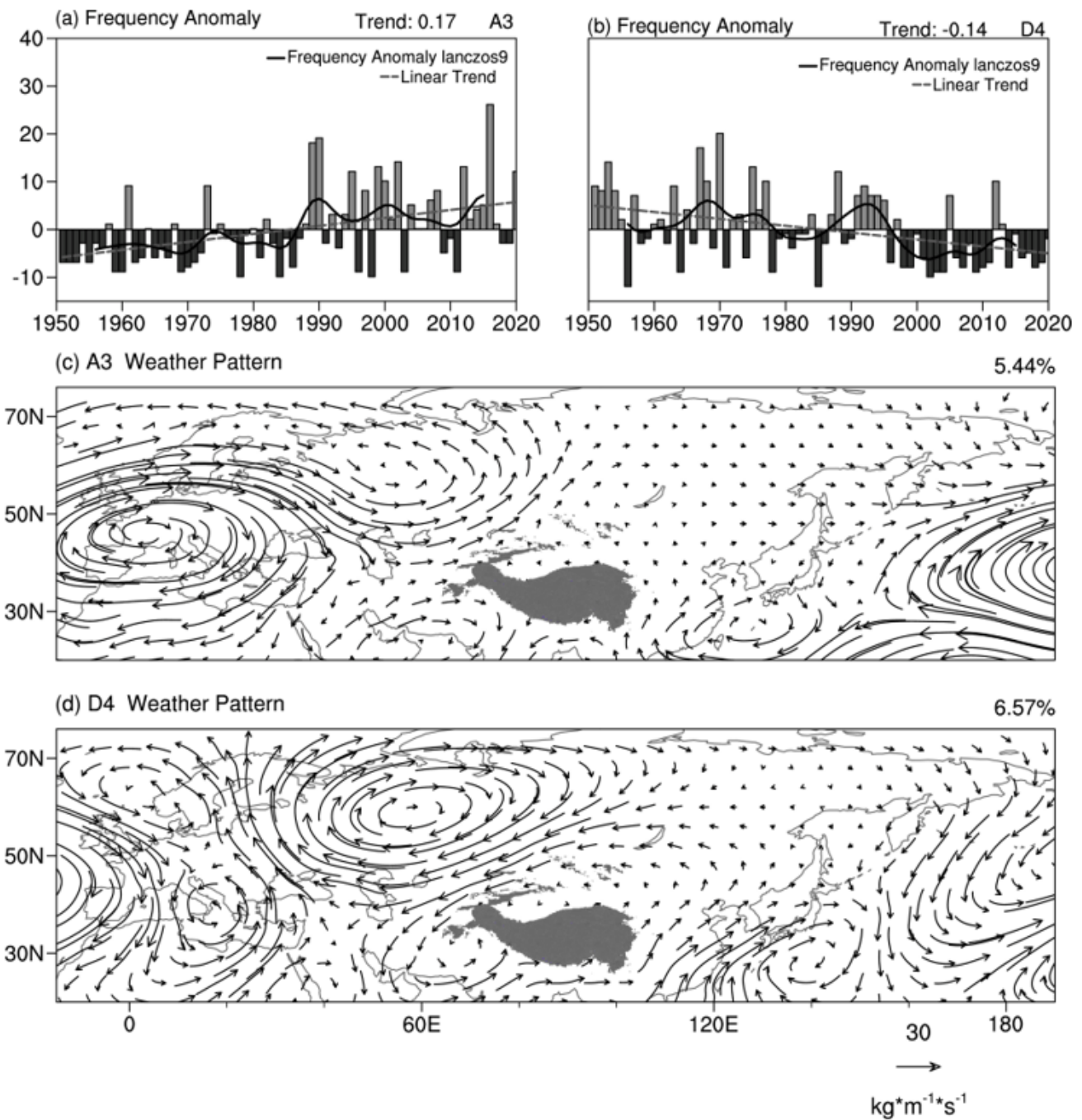
Figure 14

The A3 (c) and D4 (d) patterns (vectors; unit: 30 kg m^{-1} s^{-1}) and their percentage of days (a, b) obtained by the SOM with the global vertically integrated water vapor flux from ERA5 during 1950–2020 in the boreal winter half-year (November–April). The bars in (a, b) are the percentage of days anomalies, the curves are the 9-year low-pass filtered anomalies, and the dashed lines are the trends, which are statistically significant at the 10% level.